Controlling competing photochemical reactions stabilizes perovskite solar cells

Silvia G. Motti[1,2,6], Daniele Meggiolaro[3,4], Alex J. Barker [ID][1], Edoardo Mosconi[4], Carlo Andrea Riccardo Perini [ID][1,2], James M. Ball[1,6], Marina Gandini[1,2], Min Kim[1], Filippo De Angelis [ID][3,4,5]* and Annamaria Petrozza [ID][1]*

Metal halide perovskites have become a popular material system for fabricating photovoltaics and various optoelectronic devices. However, long-term reliability must be assured. Instabilities are manifested as light-induced ion migration and segregation, which can lead to material degradation. Discordant reports have shown a beneficial role of ion migration under illumination, leading to defect healing. By combining ab initio simulations with photoluminescence measurements under controlled conditions, we demonstrate that photo-instabilities are related to light-induced formation and annihilation of defects acting as carrier trap states. We show that these phenomena coexist and compete. In particular, long-living carrier traps related to halide defects trigger photoinduced material transformations, driving both processes. Defect formation can be controlled by blocking under-coordinated surface sites, which act as a defect reservoir. By use of a passivation strategy we are thus able to stabilize the perovskite layer, leading to improved optoelectronic material quality and enhanced photostability in solar cells.

The interest in metal halide perovskites has been growing continuously in recent years due to the remarkable evolution of their application in photovoltaics, where power conversion efficiencies exceeding 24% have been achieved[1], as well as promising performance in light-emitting diodes[2], photodetectors[3–5] and lasers[6,7]. This success owes much to their optimal optoelectronics properties, that is, their high absorption coefficients and long carrier lifetimes[8–10]. The soft nature of the lead-halide lattice induces relatively low defect formation energies, which implies a significant probability of defects formation[11] through combined thermal- and light-induced phenomena. While the impact of defects seems not to be too detrimental with respect to the figures of merit of perovskite-based devices[12], their activity poses a challenge to the widespread uptake of perovskite-based optoelectronic devices in terms of material stability under electrical and optical stimuli[13–17]. Monitoring the photoluminescence and dynamics of photogenerated charge carriers is an effective approach for gathering information about the optoelectronic properties of a semiconductor. The photoluminescence efficiency is extremely sensitive to a combination of parameters such as recombination rate constants, defect densities, carrier lifetimes and non-radiative decay paths; as such, the photoluminescence efficiency is usually taken as a measure of the material optoelectronic quality.

Since the primary function of lead halide perovskites in solar cells is to absorb light, the material response to light exposure and the possible associated phenomena are fundamental properties when creating reliable devices. A photoluminescence intensity decrease (PLID) has been observed in lead halide perovskite thin films of different composition as a result of photoinduced trap formation in inert atmosphere[18]. Enhanced photoinduced ion migration[19] has been interpreted as a defect density increase under light irradiation[20]. In direct contradiction, photoluminescence intensity enhancement (PLIE) under illumination has also been observed[21,22], which was explained by a light-induced trap annihilation mechanism[23]. A dependence of the photoluminescence efficiency variation on defect density[24] and excitation intensity[25], with both PLIE and PLID, has been reported. The atmosphere also has a strong impact on photoluminescence efficiency, with strong PLIE observed by exposing the sample to an oxygen-rich environment[18,26–30].

The presence of transient phenomena following electrical and photoexcitation and a lack of understanding of the mechanisms behind such phenomena have led to skepticism about the successful integration of lead halide perovskites in a reliable technology. From a more fundamental point of view, no general consensus exists on whether the observed transient behaviours can eventually lead to improved material quality or if they could actually destroy the material.

Here, we provide a comprehensive picture of the PLIE and PLID processes in methylammonium lead iodide (MAPbI$_3$) and bromide (MAPbBr$_3$) perovskites, showing that both phenomena can take place and compete in both materials by varying the illumination conditions, although with different characteristic times and temperature responses.
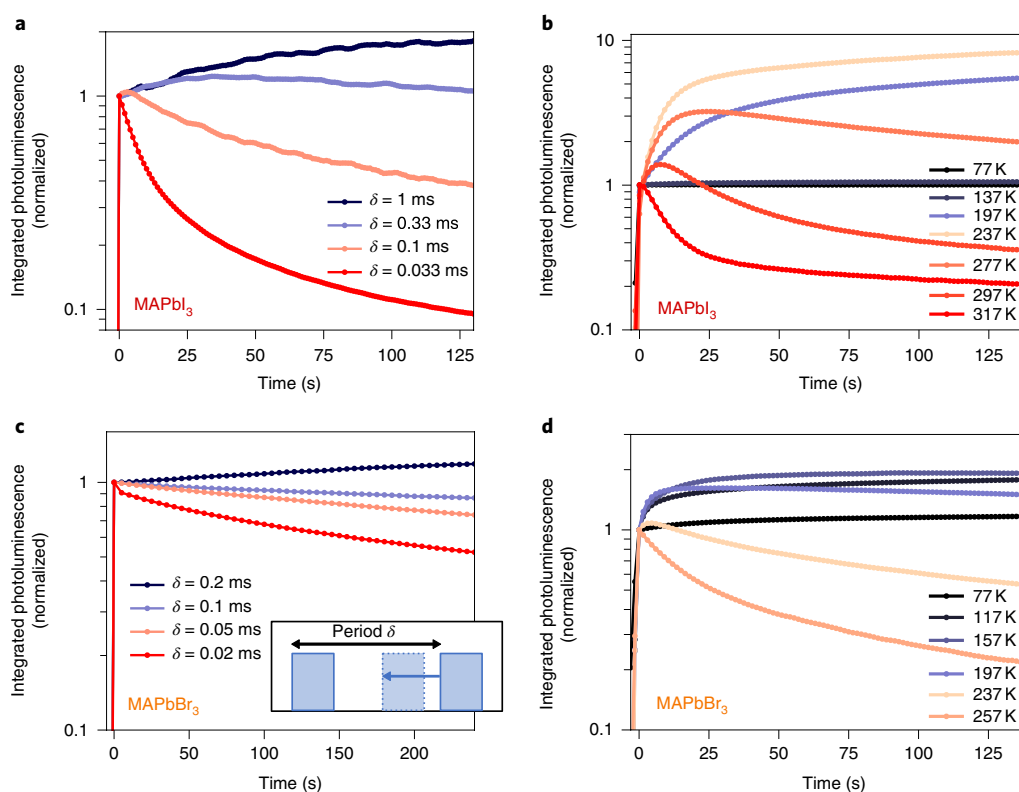
Combining our observations with first-principles calculations, we propose a model based on lead halide defect chemistry for both PLID and PLIE that consistently explains the overall phenomenology. We find that long-living carrier traps related to halide defects trigger photoinduced transformations that drive both PLIE and PLID. As long as the density of traps is relatively low or they are scarcely populated, photoinduced PLIE will be dominant, but photoinduced PLID will take over in the presence of a high density of populated traps located close to the thin-film surface and grain boundaries, which provide a reservoir of binding sites for photogenerated species, eventually leading to material

Fig. 1 | Transient integrated photoluminescence intensity from MAPbI₃ and MAPbBr₃ thin films as a function of excitation repetition rate and temperature. a,c, Integrated photoluminescence intensity, normalized at time $t = 0$, over time (excitation density ~1×10^{16} cm⁻³) on fresh spots of polycrystalline films of MAPbI₃ (**a**) and MAPbBr₃ (**c**) with increasing repetition rate (decreasing period δ) of the excitation light. The pulse width was fixed at 200 ns with constant pulse energy of 0.2 nJ (fluence of ~0.5 μJ cm², average intensity of 0.6–20 mW cm⁻²; data for a pulse width of 10 μs is shown in Supplementary Fig. 5). **b,d**, Integrated photoluminescence over time of MAPbI₃ (**b**) and MAPbBr₃ (**d**) at different temperatures under steady-state excitation (excitation intensity of ~50 mW cm⁻²). Excitation wavelength: 450 nm for MAPbI₃ and 405 nm for MAPbBr₃.

degradation. Consistent with the developed model, we show that surface passivation of MAPbI₃ thin films allows us to switch off the PLID mechanism and make the PLIE process dominant, which translates into an associated solar cell efficiency increase and enhanced temporal stability.

Results

We monitored the photoluminescence intensity of MAPbI₃ and MAPbBr₃ perovskite thin films (used in efficient solar cell devices) as a function of illumination time. Figure 1a shows the room-temperature integrated photoluminescence over time of MAPbI₃ polycrystalline films deposited on glass. The sample was excited with a laser beam incident on the film surface. The laser was modulated with a fixed pulse width of 200 ns and varying repetition rate (that is, varying the period δ between two excitation pulses). The pulse energy was kept constant to guarantee the same carrier generation density at each excitation pulse (see Supplementary Table 1 for the average excitation intensities as a function of δ). To exclude the effect of oxygen and moisture[18,27,28], all measurements were performed under active vacuum (pressure < 10⁻⁵ mbar, under a constantly running pump). We observe that the photoluminescence intensity changes over time, showing both PLIE and PLID, depending on the repetition rate for both MAPbI₃ and MAPbBr₃ (Fig. 1a,c). At low repetition rates—that is, long δ, corresponding to the sample being in the dark for periods on the scale of milliseconds—the photoluminescence intensity grows cumulatively with subsequent illumination periods. On increasing the repetition rate—short δ, corresponding to longer light exposure and less time in the dark—a quenching process kicks in, which eventually becomes dominant

(Fig. 1a). These observations clearly indicate that light absorption can lead to competing PLIE and PLID phenomena, depending on the excitation conditions. We thus performed additional experiments at varying temperatures to disentangle the factors underlying the individual phenomena involved in PLIE and PLID. Figure 1b shows the time evolution of the integrated photoluminescence intensity of a MAPbI₃ film excited with continuous-wave (c.w.) light, analogous to a very high repetition rate (that is short δ), at different temperatures. Each curve was taken on a fresh spot of the sample. For MAPbI₃, at 77 K the photoluminescence is stable for the entire duration of the experiment, and the same holds when heating the sample to 137 K. On further raising the temperature to 197 K we observe a strong PLIE over time; this is further boosted on increasing the temperature to 237 K, leading to an approximately eightfold photoluminescence increase compared to the initial value. At still higher temperature (277 K) an initial PLIE is superseded by PLID at longer exposure times, which eventually dominates at room temperature and above. Similar behaviour was observed for MAPbBr₃ films on varying the temperature, but with lower thresholds for PLID and PLIE (Fig. 1d), allowing us to safely exclude any role of structural phase transition in the observed dynamics (Supplementary Fig. 27).

The variations in photoluminescence intensity with increasing temperature, and the transition from stable photoluminescence to PLIE and to PLID, is clearly suggestive of competing thermally activated processes that either improve or hinder the efficiency of radiative recombination. The dominant contribution of PLID at higher temperature suggests a higher energy demand for this process compared to PLIE. Also, the enhanced stability range of MAPbI₃ compared to MAPbBr₃ at low temperatures (see Fig. 1b,d, with PLID
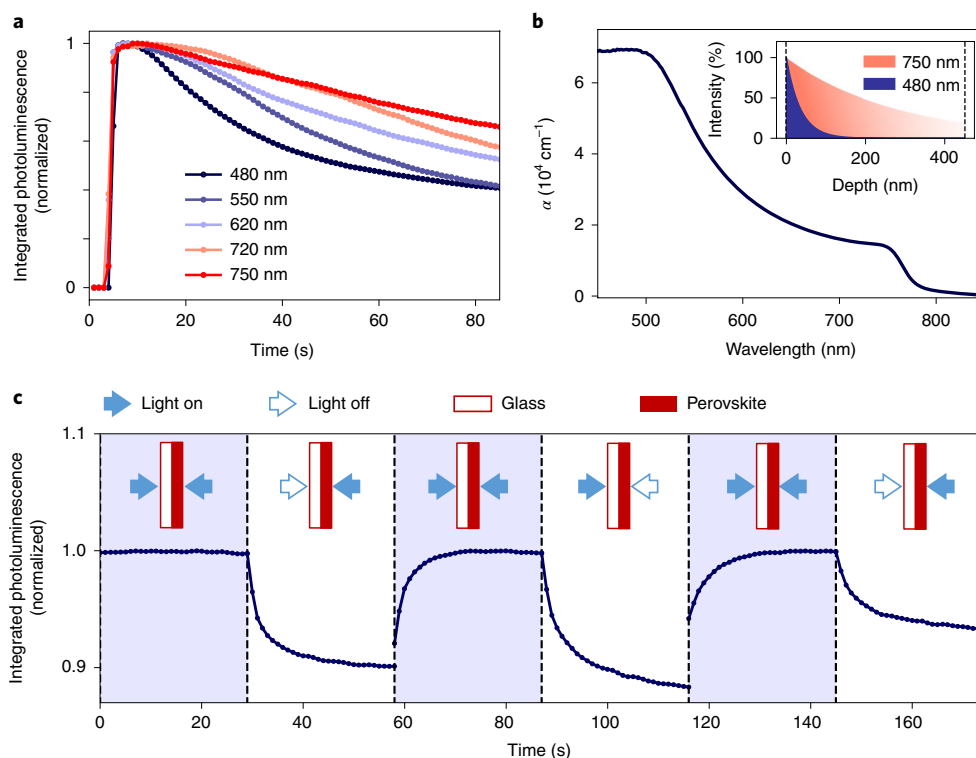
Fig. 2 | Transient integrated photoluminescence intensity from MAPbI₃ thin films as a function of excitation penetration depth and excitation geometry.
a, Integrated photoluminescence over time obtained using excitation light of different wavelengths. **b**, Absorption spectrum of MAPbI₃ thin film (see absorbance in Supplementary Fig. 28) and photoexcitation profiles when using 480 nm or 750 nm light (inset). **c**, Integrated photoluminescence intensity over time of a MAPbI₃ film on glass. Excitation is performed at 560 nm with symmetrical beams of equal intensity impinging on both the perovskite and glass side of the sample. Each section of the time trace is normalized by its maximum intensity for visualization purposes (see Supplementary Fig. 6 for unnormalized data).

starting at 277 and 197 K, respectively) suggests that the threshold for switching between the two phenomena is determined by the precise material composition, in particular by the nature of the halide.

To identify what additional factors affect the PLID and PLIE processes, we investigated the photoluminescence time evolution of MAPbI₃ as a function of the excitation wavelength, as shown in Fig. 2a. The incident photon density over the illuminated spot area was kept constant, and each curve was taken on a fresh spot of the film. We observe that PLID is significantly enhanced at shorter excitation wavelengths, while band-edge excitation results in more stable photoluminescence. Besides the additional thermal energy provided by above-gap excitation, shorter-wavelength light also has significantly shorter penetration depth (Fig. 2b). This results in a higher carrier generation close to the film surface, with a factor of ~2 increase in the first 30 nm film away from the surface in the case of 480 versus 750 nm excitation. While we cannot exclude direct excitation of PbI₂ as the cause of PLID and PLIE[30], the observation of both phenomena for MAPbBr₃ is consistent with a minor role of this phenomenon in our conditions, as excitation of the higher-bandgap (~4 eV) PbBr₂ phase only occurs at much shorter excitation wavelength than those used in our experiments. Our observations suggest that the competition between PLID and PLIE is strongly related to the illumination conditions of the thin film, which may include factors such as proximity to the reactive surface, uniformity of the excitation profile, and excitation density, with a possible contribution of thermal dissipation effects following photoexcitation.

To complement our phenomenological consideration, we investigated whether the experiment geometry could affect the relative weight of PLID versus PLIE. We find a reproducible PLIE when illuminating the film from two sides (the open surface and the glass side) with two identical beams covering a large area of the thin film, suggesting that uniform illumination may reduce the impact of PLID (Fig. 2c). Similar observations, that is, a switch from PLID to a more stable photoluminescence, are also made by varying the lateral illumination gradient (Supplementary Fig. 7).

To provide a rationale for these observations we first consider the possible role of trap-state filling, followed by de-trapping, as a possible cause determining the observed phenomenology. Despite the long lifetimes of trapped carriers in both MAPbI₃ and MAPbBr₃ (refs. [12,18,31]), extending up to several microseconds, the timescales spanned by the repetition rates in Fig. 1a are too long to be solely explained by trapping/de-trapping mechanisms. The system can reach almost a stationary density of charge carriers within the 200 ns pulse (see Supplementary Figs. 2–4 and 22–25 for simulations of charge carrier dynamics under c.w. or modulated illumination). Note that the change in modulation mainly results in a change in the averaged excitation intensity and an enhancement of the photoluminescence absolute value at time $t = 0$, due to an associated enhancement of counts during the integration (Supplementary Fig. 26). If no concomitant processes take place, though, the millisecond delay time between two consecutive pulses allows the system to return to the ground state before a second pulse comes, in contrast to the cumulative effect of pulsed illumination observed in Fig. 1a and c. At the same time, charge/lattice interaction through the formation of large polarons[32] shows lifetimes comparable to those of the charge carriers, inconsistent with the cumulative effect observed with millisecond delays. Similarly, we can rule out a role of light-induced release of lattice strain[33] in PLIE, because electronic effects are too fast to provide a cumulative effect on the millisecond repetition timescale of our experiments.

The timescales involved in PLID and PLIE are consistent with the reported ionic activities, such as ion/defect annihilation and migration rates, in both MAPbI$_3$ and MAPbBr$_3$ (refs. [23,34]) and with the timescale of photoinduced transformations in free-standing MAPbI$_3$ films[35]. Comparably, in mixed halide (I, Br) perovskites ion segregation was shown to take place via halide defects, mainly vacancies and interstitials, driven by the gradient in carrier generation through the thickness of these strongly absorbing materials[36–38]. Importantly, the observation of typical spectral features associated with trap carriers and defects in the lattice that are enhanced under c.w. illumination (Supplementary Figs. 8 and 9) is suggestive of photoinduced defect formation and annihilation being respectively related to PLID and PLIE.

With the aid of first-principles calculations we propose a model based on lead halides defect chemistry that allows us to consistently explain the observations of the data set presented above. MAPbI$_3$ and MAPbBr$_3$ show a remarkably similar defect chemistry (see Supplementary Information for a comparative analysis based on hybrid density functional theory calculations including spin–orbit coupling) that is dominated by lead vacancies (V_{Pb}) and interstitial halogen (I_i or Br_i) defects. We henceforth use this notation for defects in MAPbI$_3$—for example, I_i—but the mechanism applies similarly to MAPbBr$_3$. We notice, however, that for the latter the involved defects are somehow shallower than in MAPbI$_3$ (Supplementary Fig. 10). Both halide interstitials and lead vacancies show thermodynamic ionization levels in the bandgap. At the calculated native Fermi level, V_{Pb} is stable in the 2− charge state, so this defect could trap holes by the (−/2−) transition level, whose energy falls 0.13 eV above the valence band, while I_i^- exhibits a (0/−) charge transition 0.29 eV above the valence band. The partial shallow character of the V_{Pb} transition, less deep than I_i, and the high migration barriers associated with the diffusion of the defect ($E_a \sim 1.0$ eV)[39] highlight that this defect is only moderately active as a trap, while I_i can significantly trap both electrons and holes (Supplementary Fig. 10) through the (+/0) and (0/−) transitions. Hole trapping/de-trapping at I_i^- is a relatively fast process, while electron trapping at I_i^+ induces long living states due to the strong associated geometrical relaxation decreasing the kinetics of electron de-trapping[12,31]. The promoter of possible material transformations must be a long-living species, whose formation may trigger subsequent photochemical transformations leading to both PLID and PLIE. The most natural candidates are thus the filled electron traps with their associated lifetime of several (tens to hundreds) microseconds.

Recombination of I_i^- with V_I^+ was proposed as a means of trap annihilation[23], which restores the pristine material and decreases the concentration of traps; thus it can be associated with PLIE. Here we further disclose that long-living electrons at trapped I_i^+ defects may additionally mediate Frenkel defect annihilation.

Briefly, the formation of a $I_i^-V_I^+$ Frenkel pair in the presence of a neighbouring I_i^+ is endothermic by 0.55 eV because this process requires breaking of a Pb–I bond and displacement of the $I_i^-V_I^+$ defects (Fig. 3a). Upon electron trapping at I_i^+, which is preferentially located next to I_i^-, the system is further destabilized by 0.31 eV (Fig. 3b), adding a significant driving force to restore the pristine material. The long-living nature of the formed I_i^0, which mirrors the long electron de-trapping time, may allow sufficient time for $I_i^-V_I^+$ annihilation to effectively take place. Further insight into such a process was obtained with ab initio molecular dynamics. We start from the minimum energy geometry of an $I_i^-V_I^+$ Frenkel pair interacting with I_i^+ (Fig. 3a) and add one electron to the system, following the dynamical evolution of this globally neutral system. A sequence of ion reorganization and migration events can be visualized (Fig. 3c): (1) following electron trapping at I_i^+, confirmed by spin localization at the defect site, the system rapidly reaches the minimum energy structure of I_i^0 (blue line in Fig. 3c), increasing the I_i^0/I_i^- distance (black line); (2) V_I^+ migrates
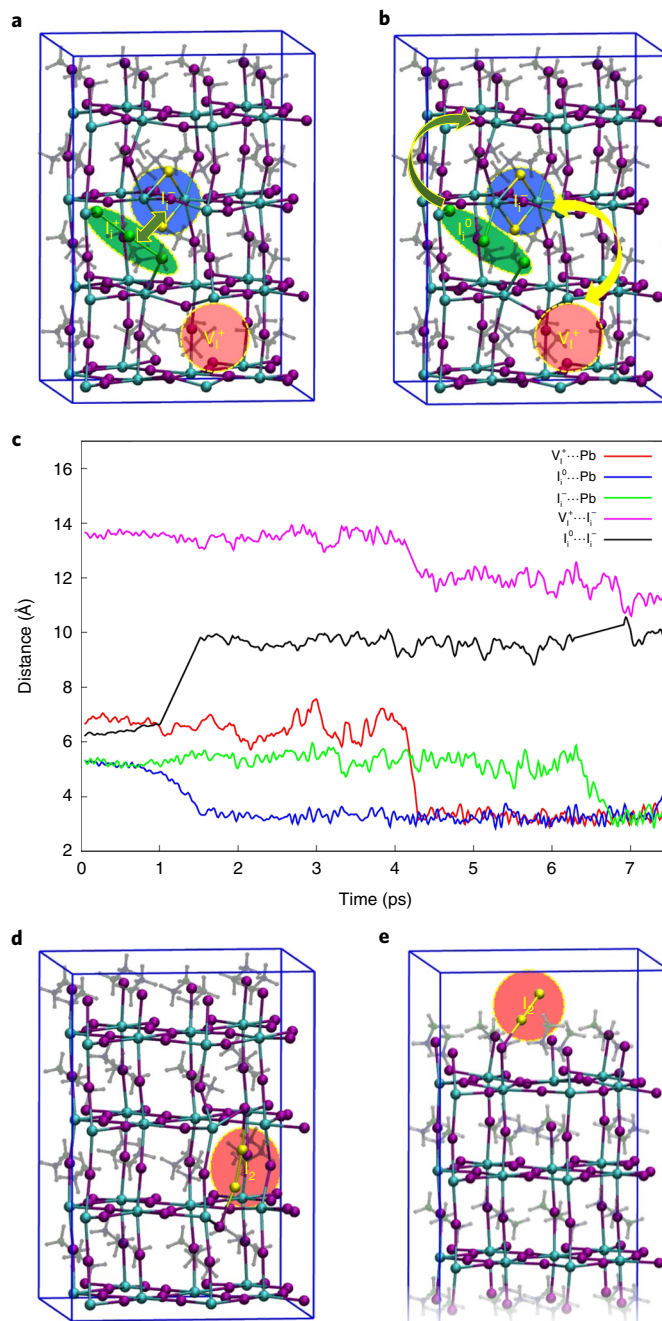

Fig. 3 | Defect dynamics. a, Optimized structure of the interacting (as signalled by the arrow) I_i^+/I_i^- defect pair (shaded green and blue areas, respectively) and a distant V_I^+ defect (shaded red area). The formation of the $I_i^-V_I^+$ defects in the presence of an interacting I_i^+ is endothermic by 0.55 eV. **b,** An electron is trapped at I_i^+ to form an I_i^0/I_i^- defect pair (shaded red and blue areas, respectively). The arrows indicate the directions of I_i^0 migration and $I_i^-V_I^+$ annihilation. The formation of the $I_i^-V_I^+$ defects in the presence of a neutral I_i^0 is endothermic by 0.86 eV. **c,** Dynamical evolution of the system after electron trapping at I_i^+. A sequence of ion reorganization and migration events can be visualized: (1) following electron trapping at I_i^+, the system rapidly reaches the minimum energy structure of I_i^0 (blue line), increasing the I_i^0/I_i^- distance (black line); (2) V_I^+ migrates in the direction of I_i^- (red and magenta lines); (3) I_i^- further migrates in the direction of V_I^+ (green and magenta lines). The dots in the legend indicate the interacting species. **d,e,** Optimized structure of an unstable bulk I_2 molecule (**d,** red shaded area), which migrates to the perovskite (001) surface in **e** to form a stable surface-bound I_2 molecule (red shaded area). Binding of an I_2 molecule to the perovskite surface (bulk) is exothermic (endothermic) by 0.48 (0.40) eV.

in the direction of I_i^- (red and magenta lines in Fig. 3c); (3) I_i^- further migrates in the direction of V_I^+ (green and magenta lines in Fig. 3c). The results are consistent with electron trapping at I_i^+ promoting I_i^--V_I^+ annihilation, as inferred from the two oppositely charged defects migrating towards each other twice within less than 10 ps. A simulation starting from the same structure but with no added electron at I_i^+ did not show any shortening of the I_i^--V_I^+ distance, although the I_i^+/I_i^- defects jointly migrated in the investigated time (Supplementary Fig. 11).

The light-induced PLIE process can be schematized as follows:

$$I_i^+/I_i^- \cdots V_I^+ + 1e \rightarrow I_i^0/I_i^- \cdots V_I^+ \rightarrow I_i^0 + prist \quad (1)$$
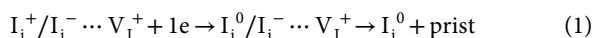
where prist represents the pristine material. Annihilation of the I_i^--V_I^+ Frenkel pair is entropically disfavoured, with a small energy barrier related to the migration of I_i^- and V_I^+ ($\sim$0.1 eV)[40]. This reaction is thus favoured at low temperature but it still requires a sufficient thermal energy to accomplish defect migration.

The de-trapping reaction

$$I_i^0 \rightarrow I_i^+ + 1e \quad (2)$$

instead has a significant activation energy (0.29 eV)[12], so the annihilation process of equation (1), mediated by the high ion mobility of iodine defects, can effectively prevail over the thermally activated detrapping of equation (2). Such a PLIE mechanism is fully consistent with the data of Fig. 1b, showing a preferential PLIE at low temperature but no PLIE if the temperature is too low to hamper defect migration. In the absence of other (PLID) processes this PLIE mechanism is cumulative because it requires a long time after de-trapping to restore the initial density of Frenkel defects due to the endothermic nature of the process, with the possible associated entropic gain hindered at low temperature. By definition, in a Frenkel defect an ion leaves its place in the lattice, creating a vacancy, and it becomes an interstitial by lodging in a nearby location, thus we expect to observe their annihilation happening even when only short-range migration is allowed (for example, at low temperature).

The PLID process is probably more complex than PLIE. We know that PLID is favoured by high illumination repetition rates. This, in turn, is associated with a larger fraction of traps being filled at any time, and possibly to a higher effective temperature due to heating of the sample. We also know from the wavelength dependence of PLID that this process is more efficient when the photogeneration happens close to the surface where a larger trap density can be envisaged. It is also amplified when ion diffusion is enhanced, that is, by the presence of gradient across dark/light regions.

A possible PLID mechanism could thus be reasonably associated to a bimolecular reaction—boosted by increasing the encountering probability of the reactants, by increasing their density and/or their mobility—occurring among the filled, long-living traps, in a film region close to the surface. Following the initiating trap-filling reaction of equation (2), two filled traps could react to form an I_2 molecule:

$$2 I_i^0 \rightarrow I_2 \quad (3)$$

This radical quenching reaction, involving two coordinated I_2^- molecules[41], takes place with virtually no energy barrier (Supplementary Fig. 12) being only limited by the diffusion of the reactants. Such a bimolecular reaction is favoured by a high trap concentration in a small volume, which increases the probability of a bimolecular encounter, as realized by the high irradiation intensity of short wavelength, as well as by allowing for long-range I_i^0 migration. The direct recombination of two interacting I_i^-/I_i^+ defects to give I_2 instead has a fairly high activation energy (0.33 eV, when calculated among surface-adsorbed species; Supplementary Fig. 13).
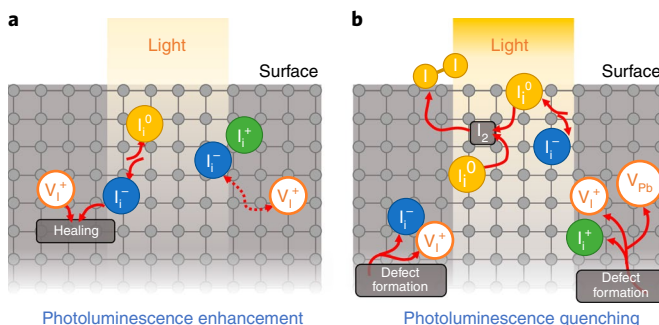
Fig. 4 | Photoluminescence enhancement and quenching mechanisms. a, Ion dynamics in MAPbI$_3$ thin film promoting PLIE (**a**), when the probability of I_0 species encounters is small and Frenkel pair annihilation is boosted by electron trapping, and PLID (**b**), when the probability of I_0 species encounters is high, boosting I_2 molecule formation.

Sequential electron and hole trapping could alternatively take place at the I_i^+/I_i^- defect pair:

$$I_i^+/I_i^- + 1e \rightarrow I_i^0/I_i^- + 1h \rightarrow 2I_i^0 \rightarrow I_2 \quad (4)$$
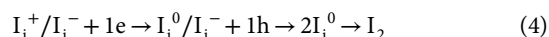
The last reaction step leads to the same I_2 product as equation (3), but its reaction probability is likely to be limited by the short-living trapped hole at I_i^-.

A filled trap may also take a second electron to form I_i^-:

$$I_i^0 + 1e \rightarrow I_i^- \quad (5)$$

The bielectronic reaction in equation (5) is favoured by high irradiation intensity. The formation of I_2 is possibly favoured over capture of a second electron, but both mechanisms can coexist. I_2 loss into toluene solution following MAPbI$_3$ light irradiation was recently reported[20], consistent with equations (3) and (4). I_2 can be trapped as a complex in the bulk (formally I_4^{2-}, Fig. 3d) or it may disproportionate to reform the I_i^+/I_i^- pair[40,42]. Importantly, both coordinated I_2 and the I_i^+/I_i^- pair tend to migrate to the surface, being stabilized by $\sim$0.4 eV. A surface-coordinated I_2 molecule represents the final reaction product (Fig. 3e). Such an I_2 molecule can remain bound to the surface or to grain boundaries. Notably I_2 can act as an electron trap, as I_i^+ does.

The iodine imbalance between surface and bulk can trigger a series of compensating reactions that regenerate the starting equilibrium distribution of I_i^+/I_i^- defects to compensate their transformation to surface-bound I_2. This can be accomplished by disrupting the pristine lattice as

$$prist \rightarrow V_{Pb}^{2-} + V_I^+ + I_i^+ \quad (6)$$
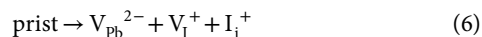
or through the formation of Frenkel pairs, according to equation (1), here simplified as

$$prist \rightarrow V_I^+ + I_i^- $$
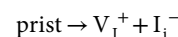
or the net reaction

$$prist \rightarrow V_{Pb}^{2-} + 2V_I^+ + I_i^- + I_i^+ \quad (7)$$
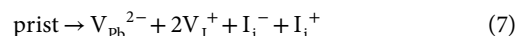
Note that $V_{Pb}^{2-} + 2V_I^+$ corresponds to the loss of PbI$_2$, which may segregate as a separate phase, with consequent material degradation[43] and associated PLID. Alternatively, metallic Pb could nucleate on the material surfaces[44].

The trigger to PLID is thus the surface (or grain boundary) stabilization of coordinated I_2. Treating the thin film with appropriate
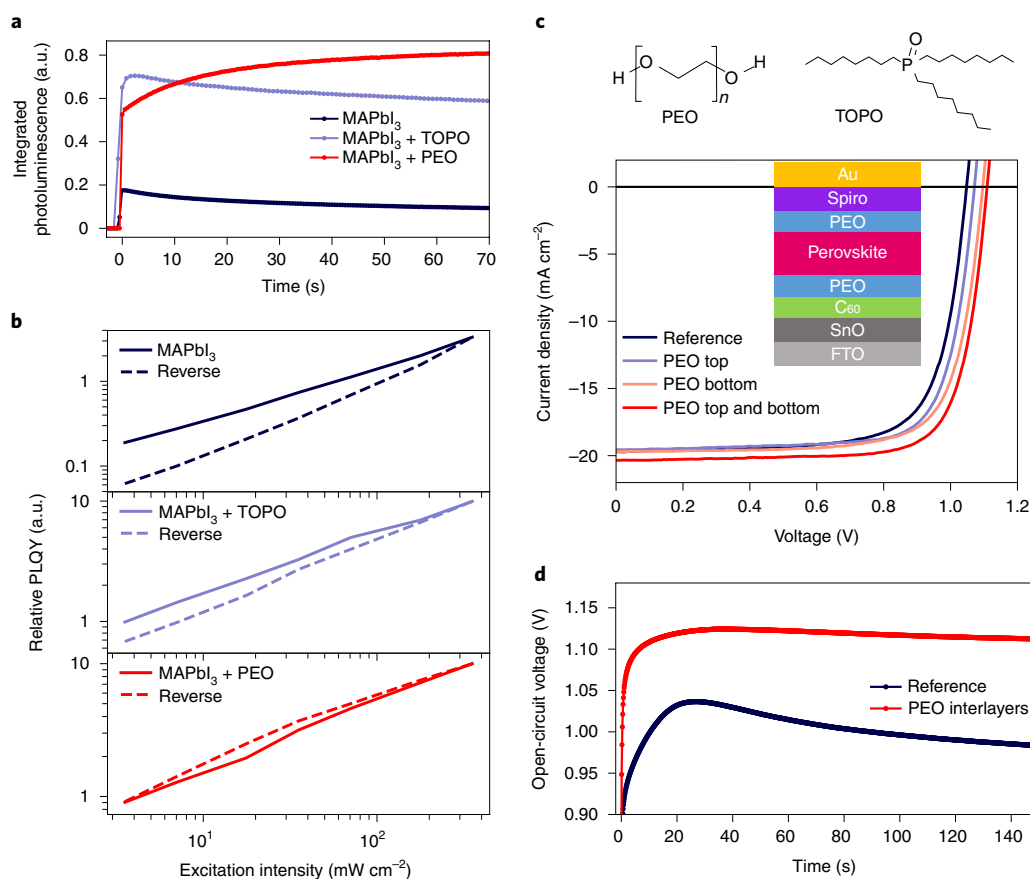
Fig. 5 | Thin film passivation. a, Photoluminescence intensity over time of MAPbI$_3$ films, bare (dark blue) or coated with TOPO (light blue) or PEO (red), taken on fresh spots (560 nm, c.w., 40 mW cm^{-2}). **b**, Relative PLQY, taken with increasing (solid lines) or decreasing (dashed lines) excitation intensities (c.w. illumination, 560 nm, hold time between data points ~30 s) of MAPbI$_3$ thin films, bare (dark blue) and coated with TOPO (light blue) or PEO (red). **c**, Current density–voltage (*J–V*) curves measured under 1 sun of MAPbI$_3$ (reference) devices with and without PEO interlayers. **d**, Open-circuit voltage (*V*$_{oc}$) transient measured from solar cells with and without PEO interlayers under 1 sun illumination.

passivating agents and blocking undercoordinated surface Pb atoms is thus the key to avoid PLID[45]. Surface passivation will result not only in an improvement of the absolute photoluminescence quantum yield of the semiconductor thin film (surface-bound I$_i^-$ is destabilized when the MAPbI$_3$ surface is capped by aliphatic ethers; Supplementary Fig. 14) but also hamper the PLID phenomenon, leaving room for PLIE to happen.

The key to blocking PLID and probably to significantly slow down perovskite degradation is passivation of the surface sites to which I$_2$ can bind in its various forms. These undercoordinated Pb surface sites, only marginally involved in trapping/de-trapping events, act as a reservoir for I$_2$, leading to iodine imbalance in the bulk and stimulating the production of additional defects. The process continues until surface sites are saturated, after which the material may start releasing I$_2$ and possibly form a segregated PbI$_2$ phase. Figure 4 summarizes the PLIE and PLID mechanisms.

To check the importance of the surface in PLID, we compared a pristine MAPbI$_3$ film with one coated with tri-*n*-octylphosphine oxide (TOPO) or polyethylene oxide (PEO) (Fig. 5a). TOPO has been applied for the passivation of perovskite films, resulting in enhanced photoluminescence efficiencies and lifetimes[10]. PEO is a polymer containing polar ether groups and hydroxyl terminations, providing a moisture barrier and a possible passivating agent[46,47]. In Fig. 5a, by illuminating a fresh spot on the samples (560 nm, c.w. excitation, fluence of ~0.1 µJ cm^{-2}) and monitoring the integrated photoluminescence signal over a few minutes, we observed a slow quenching for the bare MAPbI$_3$ thin film and an initial enhancement

followed by a slower quenching for the TOPO-passivated thin film. On the other hand, in the presence of PEO we observe that the mechanism leading to PLID is switched off even at room temperature (Fig. 5b). Despite TOPO and PEO both being characterized by the presence of oxygen atoms that interact with undercoordinated surface Pb atoms (Supplementary Fig. 14) the increased PLIE observed with PEO is suggestive of a more effective passivation by the latter, probably because of the larger fraction of oxygen atoms versus aliphatic carbon chains in PEO.

Figure 5b shows the relative photoluminescence quantum yield (PLQY), calculated as the integrated photoluminescence intensity normalized by the excitation intensity, of MAPbI$_3$ films. Each data point was taken after a hold time of ~30 s. When measuring from low to high excitation intensities (solid lines) and then in reverse order (dashed lines), we observe a hysteretic behaviour resulting from photoinduced trap formation, that is, PLID and a concomitant photoluminescence intensity reduction from bare perovskite thin films. By illuminating the film from the passivated side, both the TOPO- and PEO-coated samples show a higher photoluminescence signal, indicating a decrease in the density of native defects on the thin-film surface. Thus, also in agreement with the data shown in Fig. 5a, the sample coated with TOPO shows a less pronounced hysteretic behaviour compared to the uncoated film, while the PEO-passivated thin film presents an opposite hysteretic behaviour of the relative photoluminescence as a function of excitation intensity, as a consequence of a dominant PLIE process. This clearly shows that efficient surface passivation can reduce the density of defect states

and photostabilize the perovskite thin film. To connect our experimental and computational model, in particular the central role of surface-stabilized I_2 in PLID, we investigated the I_2-releasing reaction in hexane solution from $MAPbI_3$ films considering three cases: (1) the bare thin film; (2) $MAPbI_3$ capped by an inert polystyrene film[48]; (3) a PEO-passivated film. In line with the results of ref. [20], prolonged irradiation of the bare $MAPbI_3$ and polystyrene-capped thin films produced the same amount of I_2, while a significant reduction in I_2 production was observed for the PEO-passivated thin film (Supplementary Figs. 18–20).

The passivating PEO layer has a significant technological relevance as it allows for the formation of high-quality interlayer thin films that can be easily implemented in perovskite solar cells. In Fig. 5c we show the J–V characteristic of $MAPbI_3$-based solar cells. Here, we add PEO interlayers between the perovskite active layer and the selective charge-extracting layers. The PEO layer is seen to improve the open-circuit voltage (V_{oc}) when applied to either the electron- or hole-extracting interface, with the best performance given by the device with PEO applied to both sides (see Supplementary Table 2 for the figures of merit of the devices and Supplementary Fig. 15 for their statistics). In Fig. 5d we show the evolution of the V_{oc} of solar cells with and without the PEO interlayers under 1 sun illumination (see Supplementary Fig. 17 for monochromatic photoexcitation). The devices were encapsulated in an inert atmosphere. Despite the fact that the perovskite layer in the reference device is already interfaced with materials that have to some extent a passivating role, such as C_{60} (refs. [49,50]), we still see competing dynamics in the V_{oc} that mirror the PLID and PLIE shown in Fig. 5a. However, the relative contribution of the PLID is drastically reduced in the PEO-treated device, resulting in a higher and more stable V_{oc}.

Most notably, the PEO-passivated device also shows significantly longer stability under light soaking at the maximum power point, retaining more than 90% of its initial efficiency for 15 h, while the bare $MAPbI_3$ device loses 35% of its initial efficiency within the first 6 h (Supplementary Fig. 21).

It is worth mentioning that light-emitting diodes may operate at a relatively high density of carriers, and thus may suffer more from the PLID mechanism. As we have demonstrated, PEO interlayers are capable of passivating the perovskite surfaces, minimizing the formation of degradation products (I_2) without blocking charge injection in the device. We therefore believe that PEO could also be beneficial for light-emitting diode stability.

Conclusions

In summary, by monitoring the evolution of photoluminescence intensity under systematic control of the experimental parameters we have identified two distinct processes behind the instabilities observed in lead halide perovskites, excluding effects related to the atmosphere. We demonstrate that such processes are happening simultaneously within thin films under photoexcitation and that, depending on the conditions, one process can overcome the other, thereby reconciling the conflicting reports in the literature and providing a consistent understanding of photoinduced phenomena in this class of materials. Based on simple, yet comprehensive, experimental evidence, we are able to provide a clear model in which long-living trapped carriers—typical of halide photochemistry—mediate photoinduced ionic dynamics and lead to a dominant photoluminescence enhancement or decrease. The latter stems from a bimolecular reaction due to the encounter of two I^0 species to form I_2, and thus it is favoured in the presence of high trap density concentration and/or high temperature. The stabilization of coordinated I_2 at the surface (or grain boundary) is a fundamental factor for the efficiency loss. On the basis of this, we show that passivating the thin film surface prevents the detrimental process leading to photoluminescence decrease, favouring defect healing. This allows us to target

the relevant defect sites by passivating the semiconductor surface with PEO interlayers, improving device performance and stability.

Online content

References

1. NREL *Best Research-Cell Efficiencies* https://www.nrel.gov/pv/assets/images/efficiency-chart.png (2018).
2. Xu, W. et al. Rational molecular passivation for high-performance perovskite light-emitting diodes. *Nat. Photon.* https://doi.org/10.1038/s41566-019-0390-x (2019).
3. Lin, Q., Armin, A., Lyons, D. M., Burn, P. L. & Meredith, P. Low noise, IR-blind organohalide perovskite photodiodes for visible light detection and imaging. *Adv. Mater.* **27**, 2060–2064 (2015).
4. Wei, H. et al. Sensitive X-ray detectors made of methylammonium lead tribromide perovskite single crystals. *Nat. Photon.* **10**, 333–339 (2016).
5. Venugopalan, V. et al. High-detectivity perovskite light detectors printed in air from benign solvents. *Chem* **5**, 868–880 (2019).
6. Zhu, H. et al. Lead halide perovskite nanowire lasers with low lasing thresholds and high quality factors. *Nat. Mater.* **14**, 636–642 (2015).
7. Deschler, F. et al. High photoluminescence efficiency and optically pumped lasing in solution-processed mixed halide perovskite semiconductors. *J. Phys. Chem. Lett.* **5**, 1421–1426 (2014).
8. Stranks, S. D. et al. Electron–hole diffusion lengths exceeding 1 micrometer in an organometal trihalide perovskite absorber. *Science* **342**, 341–344 (2013).
9. Johnston, M. B. & Herz, L. M. Hybrid perovskites for photovoltaics: charge-carrier recombination, diffusion and radiative efficiencies. *Acc. Chem. Res.* **49**, 146–154 (2016).
10. deQuilettes, D. W. et al. Photoluminescence lifetimes exceeding 8 µs and quantum yields exceeding 30% in hybrid perovskite thin films by ligand passivation. *ACS Energy Lett.* **1**, 438–444 (2016).
11. Ball, J. M. & Petrozza, A. Defects in perovskite-halides and their effects in solar cells. *Nat. Energy* **1**, 16149 (2016).
12. Meggiolaro, D. et al. Iodine chemistry determines the defect tolerance of lead-halide perovskites. *Energy Environ. Sci.* **11**, 702–713 (2018).
13. Hoke, E. T. et al. Reversible photo-induced trap formation in mixed-halide hybrid perovskites for photovoltaics. *Chem. Sci.* **6**, 613–617 (2014).
14. Sanchez, R. S. et al. Slow dynamic processes in lead halide perovskite solar cells. Characteristic times and hysteresis. *J. Phys. Chem. Lett.* **5**, 2357–2363 (2014).
15. Leijtens, T. et al. Mapping electric field-induced switchable poling and structural degradation in hybrid lead halide perovskite thin films. *Adv. Energy Mater.* **5**, 1–11 (2015).
16. Gottesman, R. et al. Photoinduced reversible structural transformations in free-standing $CH_3NH_3PbI_3$ perovskite films. *J. Phys. Chem. Lett.* **6**, 2332–2338 (2015).
17. Gottesman, R. & Zaban, A. Perovskites for photovoltaics in the spotlight: photoinduced physical changes and their implications. *Acc. Chem. Res.* **49**, 320–329 (2016).
18. Motti, S. G. et al. Photoinduced emissive trap states in lead halide perovskite semiconductors. *ACS Energy Lett.* **1**, 726–730 (2016).
19. Xing, J. et al. Ultrafast ion migration in hybrid perovskite polycrystalline thin films under light and suppression in single crystals. *Phys. Chem. Chem. Phys.* **18**, 30484–30490 (2016).
20. Kim, G. Y. et al. Large tunable photoeffect on ion conduction in halide perovskites and implications for photodecomposition. *Nat. Mater.* **17**, 445–449 (2018).
21. deQuilettes, D. W. et al. Photo-induced halide redistribution in organic–inorganic perovskite films. *Nat. Commun.* **7**, 11683 (2016).
22. Stranks, S. D. et al. Recombination kinetics in organic–inorganic perovskites: excitons, free charge and subgap states. *Phys. Rev. Appl.* **2**, 034007 (2014).
23. Mosconi, E., Meggiolaro, D., Snaith, H. J., Stranks, S. D. & De Angelis, F. Light-induced annihilation of Frenkel defects in organo–lead halide perovskites. *Energy Environ. Sci.* **9**, 3180–3187 (2016).
24. Chen, S. et al. Light illumination induced photoluminescence enhancement and quenching in lead halide perovskite. *Sol. RRL* **1**, 1600001 (2017).
25. Hong, D. et al. Nature of photo-induced quenching traps in methylammonium lead triiodide perovskite revealed by reversible photoluminescence decline. *ACS Photon.* **5**, 2034–2043 (2018).
26. Fang, H.-H. et al. Ultrahigh sensitivity of methylammonium lead tribromide perovskite single crystals to environmental gases. *Sci. Adv.* **2**, e1600534 (2016).

27. Galisteo-López, J. F., Anaya, M., Calvo, M. E. & Míguez, H. Environmental effects on the photophysics of organic–inorganic halide perovskites. *J. Phys. Chem. Lett.* **6**, 2200–2205 (2015).

28. Tian, Y. et al. Mechanistic insights into perovskite photoluminescence enhancement: light curing with oxygen can boost yield thousandfold. *Phys. Chem. Chem. Phys.* **17**, 24978–24987 (2015).

29. Meggiolaro, D., Mosconi, E. & De Angelis, F. Mechanism of reversible trap passivation by molecular oxygen in lead–halide perovskites. *ACS Energy Lett.* **2**, 2794–2798 (2017).

30. Quitsch, W.-A. et al. The role of excitation energy in photobrightening and photodegradation of halide perovskite thin films. *J. Phys. Chem. Lett.* **9**, 2062–2069 (2018).

31. Leijtens, T. et al. Carrier trapping and recombination: the role of defect physics in enhancing the open circuit voltage of metal halide perovskite solar cells. *Energy Environ. Sci.* **9**, 3472–3481 (2016).

32. Miyata, K. et al. Large polarons in lead halide perovskites. *Sci. Adv.* **3**, e1701217 (2017).

33. Tsai, H. et al. Light-induced lattice expansion leads to high-efficiency perovskite solar cells. *Science* **360**, 67–70 (2018).

34. Azpiroz, J. M., Mosconi, E., Bisquert, J. & De Angelis, F. Defect migration in methylammonium lead iodide and its role in perovskite solar cell operation. *Energy Environ. Sci.* **8**, 2118–2127 (2015).

35. Gottesman, R. et al. Extremely slow photoconductivity response of $CH_3NH_3PbI_3$ perovskites suggesting structural changes under working conditions. *J. Phys. Chem. Lett.* **5**, 2662–2669 (2014).

36. Barker, A. J. et al. Defect-assisted photoinduced halide segregation in mixed-halide perovskite thin films. *ACS Energy Lett.* **2**, 1416–1424 (2017).

37. Brennan, M. C., Draguta, S., Kamat, P. V. & Kuno, M. Light-induced anion phase segregation in mixed halide perovskites. *ACS Energy Lett.* **3**, 204–213 (2018).

38. Yoon, S. J., Kuno, M. & Kamat, P. V. Shift happens. How halide ion defects influence photoinduced segregation in mixed halide perovskites. *ACS Energy Lett.* **2**, 1507–1514 (2017).

39. Eames, C. et al. Ionic transport in hybrid lead iodide perovskite solar cells. *Nat. Commun.* **6**, 7497 (2015).

40. Meggiolaro, D., Mosconi, E. & De Angelis, F. Modeling the interaction of molecular iodine with $MAPbI_3$: a probe of lead–halide perovskites defect chemistry. *ACS Energy Lett.* **3**, 447–451 (2018).

41. Boschloo, G. & Hagfeldt, A. Characteristics of the iodide/triiodide redox mediator in dye-sensitized solar cells. *Acc. Chem. Res.* **42**, 1819–1826 (2009).

42. Zhang, L. & Sit, P. H.-L. Ab initio study of the role of oxygen and excess electrons in the degradation of $CH_3NH_3PbI_3$. *J. Mater. Chem. A* **5**, 9042–9049 (2017).

43. Wang, S., Jiang, Y., Juarez-Perez, E. J., Ono, L. K. & Qi, Y. Accelerated degradation of methylammonium lead iodide perovskites induced by exposure to iodine vapour. *Nat. Energy* **2**, 16195 (2016).

44. Sadoughi, G. et al. Observation and mediation of the presence of metallic lead in organic–inorganic perovskite films. *ACS Appl. Mater. Interfaces* **7**, 13440–13444 (2015).

45. Noel, N. K. et al. Enhanced photoluminescence and solar cell performance via Lewis base passivation of organic–inorganic lead halide perovskites. *ACS Nano* **8**, 9815–9821 (2014).

46. Ling, Y. et al. Enhanced optical and electrical properties of polymer-assisted all-inorganic perovskites for light-emitting diodes. *Adv. Mater.* **28**, 8983–8989 (2016).

47. Wang, Z. et al. Efficient and stable pure green all-inorganic perovskite $CsPbBr_3$ light-emitting diodes with a solution-processed NiO_x interlayer. *J. Phys. Chem. C* **121**, 28132–28138 (2017).

48. Kim, M., Motti, S. G., Sorrentino, R. & Petrozza, A. Enhanced solar cell stability by hygroscopic polymer passivation of metal halide perovskite thin film. *Energy Environ. Sci.* **11**, 2609–2619 (2018).

49. Xu, J. et al. Perovskite–fullerene hybrid materials suppress hysteresis in planar diodes. *Nat. Commun.* **6**, 7081 (2015).

50. Shao, Y., Xiao, Z., Bi, C., Yuan, Y. & Huang, J. Origin and elimination of photocurrent hysteresis by fullerene passivation in $CH_3NH_3PbI_3$ planar heterojunction solar cells. *Nat. Commun.* **5**, 5784 (2014).

Author contributions
S.G.M. performed the photoluminescence measurements. D.M. and E.M. performed the first-principles calculations. C.A.R.P., J.M.B., M.G. and M.K. were responsible for fabrication of the thin films. M.K. fabricated the solar cell devices and M.K and A.J.B. characterized the solar cell. A.P., S.G.M., A.J.B., D.M. and F.D.A. analysed the data. S.G.M., F.D.A. and A.P. wrote the first draft of the manuscript and all authors contributed to the discussions and finalized the manuscript. A.P. supervised the project.

Competing interests
The authors declare no competing interests.

Additional information
Supplementary information is available for this paper at https://doi.org/10.1038/s41566-019-0435-1.

Reprints and permissions information is available at www.nature.com/reprints.

Correspondence and requests for materials should be addressed to F.D.A. or A.P.

Publisher's note: Springer Nature remains neutral with regard to jurisdictional claims in published maps and institutional affiliations.

Methods

Sample preparation. Lead(II) bromide (PbBr$_2$, ≥98%), *N,N*-dimethylformamide (DMF, anhydrous, 99.8%), chlorobenzene (anhydrous, 99.8%) and dimethyl sulfoxide (DMSO, anhydrous, ≥99.9%) were purchased from Sigma-Aldrich; methylammonium bromide (MABr) and methylammonium iodide (MAI) were purchased from Dyesol; lead(II) iodide (PbI$_2$, 99.9985%, CAS no. 10101-63-0) was purchased from Alfa Aesar. All chemicals were used without any further purification. Glass substrates were cleaned in acetone and isopropyl alcohol (IPA) for 10 min by sonication. The cleaned glass substrates were treated with oxygen plasma for 10 min before any further deposition.

MAPbBr$_3$ thin films. These films could be fabricated by an adapted nanocrystal-pinning technique[51]. In this case, two steps of spin-coating speed were used (500 r.p.m. for 7 s, 3,000 r.p.m. for 90 s). After spin-speed acceleration, a solution of MABr and PbBr$_2$ (molar ratio 1.05:1) in DMSO was spin-coated onto the clean glass substrate. After 60 s, pinning occurred by dropping 300 μl of chlorobenzene onto the spinning sample. The samples were then baked at 90 °C for 10 min.

MAPbI$_3$ thin films. These films were fabricated by quenching a precursor solution with an antisolvent during spin coating[52], in a nitrogen-filled glovebox. A 1.45 M precursor solution of PbI$_2$:MAI:DMSO in a molar ratio of 1:1:1 was prepared in DMF. This solution was spin-coated onto the glass substrate at 4,000 r.p.m., with an acceleration of 4,000 r.p.m. s^{-1}, for 15 s. After 6 s, toluene (an antisolvent to the precursor solution) was dropped onto the spinning sample by pipette. The samples were then annealed at 100 °C for 10 min.

MAPbI$_3$ thin films with passivation. TOPO or PEO was dissolved in anhydrous chlorobenzene at a concentration of 10 mg ml^{-1}. Solutions were sonicated for 10 min for complete dissolution before deposition on top of the perovskite film by spin-coating at 4,000 r.p.m.

Device fabrication. *Film fabrication.* Indium tin oxide (ITO) on a glass substrate was etched with 2 M aqueous HCl solution and zinc powder (Sigma Aldrich). The ITO substrates were sequentially washed with 2% Hellamanex in deionized water, deionized water, isopropanol, acetone, isopropanol in a sonication bath, followed by O$_2$ plasma cleaning for 10 min. The cleaned ITO substrate was covered with a SnO$_2$ layer (~20 nm) by spin-coating of a diluted SnO$_2$ nanoparticle solution (Alfa Aesar) and annealed at 180 °C for 1 h. On the SnO$_2$ layer, a C$_{60}$ layer was deposited from a C$_{60}$ solution (10 mg ml^{-1}) in 1,2-dichlorobenzene by spin-coating at 3,000 r.p.m., followed by thermal annealing at 100 °C for 10 min. The perovskite layer was fabricated by applying an anti-solvent quenching method. For the hole transport layer, a spiro-MeOTAD solution was spin-coated on the perovskite layer at 4,000 r.p.m. for 30 s. Spiro-MeOTAD solution was prepared by dissolving 73 mg of spiro-MeOTAD in 1 ml chlorobenzene (99.8%, Sigma-Aldrich), to which was added 28.8 μl of 4-*tert*-butylpyridine (96%, Sigma-Aldrich), 17.5 μl lithium bis(trifluoromethanesulfonyl)imide (LiTFSI) solution (520 mg LiTSFI in 1 ml acetonitrile, 99.8%, Sigma-Aldrich). This fabrication process was carried out under controlled conditions in a glove-box atmosphere. Finally, 75 nm gold was thermally evaporated on top of the device at a pressure of 1 × 10^{-6} mbar to form the top-contact electrode.

Solar cell characterization. All devices were measured under simulated AM1.5 solar illumination using a class AAA solar simulator (Oriel Sol3A, Newport). The illumination intensity was calibrated using an unfiltered certified Si reference diode (area = 4 cm^2, Newport) to be 100 mW cm^{-2} (typical spectral mismatch factor of 1.01 for solar cells based on CH$_3$NH$_3$PbI$_3$). The current density–voltage (*J–V*) characteristics were recorded with a Keithley 2440. No light soaking or pre-biasing was applied before the *J–V* measurements. The illuminated electrode area, defined with a holed black anodized aluminium mask, was 0.0935 cm^2. Devices were measured in an ambient atmosphere at 23 ± 2 °C and 40–60% relative humidity. The scan rates of the *J–V* sweep were 0.2 V s^{-1}. The forward scan was from 0 V (the short-circuit condition) to 1.4 V, and the backward scan was from 1.4 V to 0 V. The stability of the current/power output with time was recorded for 120 s. The external quantum efficiency was measured with a home-built set-up. The external quantum efficiency spectra were recorded using the monochromated (Bentham) output from a tungsten halogen lamp calibrated with a Newport UV-818 photodiode.

Transient open-circuit voltage measurements. The excitation source was simulated AM1.5 solar illumination produced using a class AAA solar simulator (Oriel Sol3A, Newport) or an unfocused beam of a 450 nm c.w. diode laser (Oxxius). The beam was expanded to match the active area of the device (~0.1 cm^2) and the excitation power density was ~100 mW cm^{-2}. The devices

were encapsulated using epoxy and glass, and then mounted perpendicular to the excitation. A Keithley 2401 instrument was used to measure the transient open-circuit voltage over a duration of ~1,500 s.

Modulation frequency-dependent photoluminescence. Excitation was provided with a c.w. diode laser (Oxxius laserboxx). The excitation wavelength was 405 nm for MAPbBr$_3$ films and 450 nm for MAPbI$_3$. Modulation was accomplished using a waveform generator connected directly to the laser. Pulse widths were kept fixed to exclude the effects of varying illumination times so we could probe only the dependence on the intervals in the dark. MAPbI$_3$ films were illuminated with pulses of 200 ns at frequencies of 1, 3, 10 and 30 kHz. MAPbBr$_3$ films were illuminated with pulses of 10 μs and frequencies of 50, 500 and 5 kHz. The excitation fluences used were ~0.5 μJ cm^{-2}, corresponding to an excitation density of ~1 × 10^{16} cm^{-3}. Samples were mounted inside a vacuum chamber mounted on a translation stage that allowed fresh spots to be probed between every curve by changing the sample height without damaging the collection alignment. Photoluminescence was collected in reflection mode and focused into a fibre coupled to a spectrometer (Ocean Optics Maya Pro 2000).

Temperature-dependent photoluminescence. Excitation was provided with a c.w. diode laser (Oxxius laserboxx). The excitation wavelength was 405 nm for MAPbBr$_3$ films and 450 nm for MAPbI$_3$. The excitation intensity was ~50 mW cm^{-2}, corresponding to an estimated excitation density ~1 × 10^{16} cm^{-3}. Films were mounted in vacuum in a cold finger cryostat cooled with liquid N$_2$ (Oxford Instruments), perpendicular to the excitation line. The excitation beam was directed to the sample by a dichroic mirror and photoluminescence was collected in reflection mode and focused into a fibre coupled to a spectrometer (Ocean Optics Maya Pro 2000).

Double-sided illumination. The beam of a 560 nm c.w. diode laser (Oxxius) was expanded and collimated with a telescope to a diameter of ~3 mm. A beamsplitter was used to obtain the two excitation lines and attenuators were used to balance the intensities. Samples were mounted inside a vacuum chamber (pressure below 1 × 10^{-5} mbar) and photoluminescence was collected at a right angle to the excitation line and focused into a fibre coupled to a spectrometer (Ocean Optics Maya Pro 2000).

Photoluminescence on passivated samples. The excitation source was an unfocused beam of a 560 nm c.w. diode laser (Oxxius). Samples were mounted inside a vacuum chamber (pressure below 1 × 10^{-5} mbar) and photoluminescence was collected in reflection mode at a right angle from the excitation line and focused into a fibre coupled to a spectrometer (Ocean Optics Maya Pro 2000). Integrated photoluminescence over time was measured on fresh spots of the film with an intensity of ~40 mW cm^{-2}.

For relative PLQY measurements, the integrated photoluminescence was measured at varying excitation intensities and plotted as

$$\text{Relative PLQY} = \frac{I_{\text{PL}}}{I_{\text{pump}}}$$

Excitation wavelength dependence. The excitation source was a supercontinuum laser (SuperK Extreme, NKT Photonics), spectrally filtered by an acousto-optic modulator (SuperK Select, NKT Photonics). The selected output was directed to a home-built transmission microscope in a confocal configuration. The sample was placed on top of a piezoelectric translation stage. The photoluminescence transients (Fig. 2a) were taken by tuning the wavelength of the acousto-optic modulator output and monitoring the photoluminescence over time with a spectrometer (Ocean Optics Maya Pro 2000) coupled to the microscope for detection.

Data availability

The data that support the plots within this paper and other findings of this study are available from the corresponding authors on reasonable request.

References

51. Cho, H. et al. Overcoming the electroluminescence efficiency limitations of perovskite light-emitting diodes. *Science* **350**, 1222–1225 (2015).
52. Xiao, M. et al. A fast deposition–crystallization procedure for highly efficient lead iodide perovskite thin-film solar cells. *Angew. Chem. Int. Ed.* **126**, 10056–10061 (2014).